

# Variational inference for pile-up removal at hadron colliders with diffusion models

Malte Algren,<sup>1,\*</sup> Christopher Pollard,<sup>2,†</sup> John Andrew Raine,<sup>1,‡</sup> and Tobias Golling<sup>1</sup>

<sup>1</sup>*Département de physique nucléaire et corpusculaire, University of Geneva, Geneva 1211 Switzerland*

<sup>2</sup>*Department of physics, University of Warwick, Coventry CV4 7AL, United Kingdom*

In this paper, we present a novel method for pile-up removal of  $pp$  interactions using variational inference with diffusion models, called VIPR. Instead of using classification methods to identify which particles are from the primary collision, a generative model is trained to predict the constituents of the hard-scatter particle jets with pile-up removed. This results in an estimate of the full posterior over hard-scatter jet constituents, which has not yet been explored in the context of pile-up removal. We evaluate the performance of VIPR in a sample of jets from simulated  $t\bar{t}$  events overlain with pile-up contamination. VIPR outperforms SOFTDROP in predicting the substructure of the hard-scatter jets over a wide range of pile-up scenarios.

## I. INTRODUCTION

Hadron colliders, such as the Large Hadron Collider [1] (LHC) at CERN, deliver unrivalled centre of mass energies for partonic collisions (at least by contemporary standards) and therefore give access to processes at previously unexplored kinematic extremes. The intensity of proton bunches at the LHC yields many inelastic  $pp$  collisions per beam crossing [2, 3]; this is necessary to produce rare and energetic processes at appreciable rate. Most  $pp$  interactions occur at low center-of-mass energies [4, 5] – well below those required to produce  $W$  and  $Z$  bosons, the Higgs boson, and the top quark [6] – and recording all such collisions is not feasible with current detector readout systems and computing infrastructure [7, 8].

When a collision of interest (the “hard-scatter” interaction), e.g. one involving a final-state top quark, is produced in a bunch crossing, these additional inelastic  $pp$  interactions (known as “pile-up” interactions) each produce relatively low-momentum hadrons and photons, resulting in extra energy depositions in the detector unrelated to the physics of the hard-scatter process. Cur-

rently, the ATLAS [9] and CMS [10] experiments record collisions at a maximum instantaneous number of interactions per crossing ( $\mu$ ) of approximately  $\mu = 80$ , with a maximum  $\mu$  averaged over several minutes of about  $\langle\mu\rangle = 60$  [11]. However, as the LHC enters the high luminosity phase,  $\langle\mu\rangle$  is expected to increase to between 130 and 200 [12]. Having a large number of pile-up interactions coincident with a collision of interest yields a challenging environment for certain signatures. For example, the reconstruction of charged particle tracks and primary interaction vertices degrade with the density and multiplicity of pile-up interactions [13, 14].

Particles from pile-up interactions also contaminate hadronic jets (“jets”) originating from the hard-scatter interaction, and the mitigation of this contamination is critical for achieving acceptable resolution of relevant jet observables.<sup>1</sup>

Several techniques have been developed to reduce the impact of pile-up particles on jet observables. The SOFT-KILLER and PUPPI algorithms attempt to identify and remove individual pile-up particles before jet reconstruction begins [16, 17], while other strategies involve remov-

\* malte.algren@unige.ch

† christopher.pollard@warwick.ac.uk

‡ john.raine@unige.ch

<sup>1</sup> See Ref. [15] for an overview of jet clustering algorithms used in present-day collider experiments and their theoretical motivation.

ing jet constituents from pile-up interactions only after clustering has taken place [18–23]. Methods have also been developed to identify and remove entire jets that are determined to originate primarily from pile-up [24, 25]. In recent years, machine learning-based approaches have been deployed and studied in a variety of these contexts [26–31].

Hadronic jets come in many shapes and sizes, and several approaches to jet reconstruction are currently in use by LHC experiments. The ATLAS and CMS collaborations primarily utilize the anti- $k_t$  jet clustering algorithm with radius parameter  $R = 0.4$  to collect hadrons from the fragmentation of high-momentum gluons and quarks with low masses relative to the  $pp$  collision energy ( $u, d, c, s, b$ ) [6]. Jet algorithms with larger radius parameters have proven successful for the reconstruction and identification of hadronic decays of particles whose momenta transverse to the proton beam ( $p_T$ ) are on the order of the of the decaying particle’s mass ( $m$ ):  $m/p_T \sim 1$ . This approach allows decay products to be treated coherently as part of a single object (sometimes referred to as a “boosted” reconstruction strategy) rather than using several smaller-radius jets as a proxies for a subset of partonic decay products (a “resolved” reconstruction strategy). The boosted reconstruction strategy has been shown to achieve strong rejection of background processes at a given signal efficiency, taking advantage of the discriminating power of the internal structure (“sub-structure”) of the large-radius jet. This approach has been studied in depth for high-momentum vector bosons, Higgs bosons, and top quarks in both phenomenological and experimental settings [32–36].

The effective area of anti- $k_t$  jets in the detector, and therefore the amount of pile-up contamination, grows with the jet algorithm radius parameter [15]; the presence of pile-up can substantially alter measurements of large-radius jets in particular. Observables that depend strongly on the angular separation of jet constituents relative to the jet axis, such as the jet mass [37], are sen-

sitive to pile-up since pile-up particles tend to be more evenly spread throughout the jet area than those from a resonance decay. Dedicated algorithms have been developed to mitigate this pile-up contribution, and many of these techniques also work to remove contributions from the underlying event. Section 4.2 of Ref [38] in particular provides a useful resource for a comparison across several of them.

In this work we introduce a new method, called variational inference for pile-up removal (VIPR), which exploits diffusion models [39–41] in order to infer the true constituents of a jet originating from the hard scatter interaction based its observed jet that has been contaminated by pile-up. Diffusion models are well suited to generate unordered set of constituents which comprise jets, and have already been demonstrated to provide state-of-the-art performance in high energy physics [42–56]. Rather than produce a single estimate of jet observables, we approximate the full posterior distribution over jet constituents, from which a wide array of observables may be built; this posterior includes variations over jet constituent multiplicities. VIPR generates samples of pile-up-free hard-scatter jets from this posterior, complete with individual constituent information, that are consistent with an *observed jet* containing a combination of hard-scatter and pile-up contributions. A population of these samples faithfully represents the relative probabilities of pure hard-scatter jets that may have produced the observed jet.

To illustrate the method and to quantify its performance for a concrete process of interest at the LHC, we overlay particles from pile-up collisions onto large-radius jets in  $t\bar{t}$  events from  $pp$  collisions at 14 TeV. We use VIPR to approximate the posterior over particle-level constituents of large-radius jets from high- $p_T$  top-quark decays, given an observation composed of jets contaminated by the pile-up overlay. We benchmark our method against the standard SOFTDROP grooming algorithm [18], and show that VIPR yields an unbiased es-

timate of the hard-scatter jet mass,  $p_T$ , and substructure observables over a wide range of pile-up conditions for  $50 < \mu < 250$ , whereas SOFTDROP does not. We also find that the resolution of the VIPR posterior tends to be considerably narrower than that of SOFTDROP across all evaluated  $\mu$  values. Additionally, we find the coverage of VIPR in these quantities to be conservative estimate of ground truth jet observables.

## II. SIMULATED DATASET

In this work we study the impact of pile-up and pile-up removal techniques on large radius jets and their substructure using large radius jets initiated by boosted top quarks.

Samples of simulated  $t\bar{t}$  events in which both top quarks decay hadronically are generated using MadGraph5\_aMC@NLO [57] (v3.1.0). The decays of the top quarks and  $W$  bosons are performed using MadSpin [58], with the top quarks required to have  $p_T > 450$  GeV. The parton shower and hadronisation is subsequently performed with PYTHIA [59] (v8.243) using the NNPDF2.3LO PDF set [60] with  $\alpha_S(m_Z) = 0.130$  using the LHAPDF [61] framework.

To avoid costly resimulation and reclustering of the jets for different pile-up conditions, interactions with the detector are not performed, this is in line with many previous studies [16, 17, 26, 27, 30]. Instead we consider all visible final state particles after the parton shower arising from the hard scatter event and pile-up collisions.

The particles in the  $t\bar{t}$  events are clustered into jets using the anti- $k_t$  algorithm [62] with  $R = 1.0$  using the FastJet [63] implementation, and each of the two resulting jets (“top jets”) are considered independently. A minimum  $p_T$  requirement of 500 MeV is applied to the jet constituents before clustering. These top jets without pile-up contamination are considered the ground truth for all studies.

To simulate various scenarios for the number of interac-

tions in a crossing of LHC bunches,  $\mu$ , inclusive inelastic proton-proton collisions (IICs) produced with PYTHIA are overlain on the simulated  $t\bar{t}$  events. A collection of 500,000 IICs were produced, and to simulate  $\mu$  interactions in a bunch crossing,  $\mu - 1$  IICs are drawn from this collection. Each IIC is rotated by a random uniform azimuthal angle  $\phi$  and randomly mirrored across the  $xy$  plane (i.e. the  $z$ -coordinate is transformed by  $z \rightarrow -z$ ) in order to improve the statistical power of the IIC sample.

The resulting final-state particles which fall within the radius of the top jet are appended to the jet constituents; only particles with  $E > 500$  MeV are included. This process is performed independently for each jet and value of  $\mu$ , and jets after this pile-up overlay are called “observed jets”.

In total there are about 1 million simulated top jets and 500,000 IICs. The top jets are split into train, test and validation samples, making up 70%, 19.5% and 10.5% of the total sample, respectively.

## III. METHOD

VIPR follows the EDM diffusion scheme described in Ref. [41]. We aim to derive a generative model to approximate

$$p(\{\vec{c}_{true}\} | S, \{\vec{c}_{obs}\}, \mu) \quad (1)$$

where the notation  $\{\cdot\}$  indicates a homogeneous unordered set,  $\{\vec{c}_{true}\}$  are the desired inferred observables for hard-scatter constituents of the jet,  $S$  represents observed summary quantities of the jet in question,  $\{\vec{c}_{obs}\}$  are the observed quantities for each jet constituent, and  $\mu$  is the number of pile-up interactions in a bunch-crossing. This approach differs from deterministic machine learning-based approaches [26–31] that formulate the problem as a classification task for removing individual constituents directly from the observed jet. In this study we focus on the case where  $\{\vec{c}_{true}\}$  and  $\{\vec{c}_{obs}\}$  are simply constituent three-momenta and leave other parti-

cle quantities such as charge, species, etc. for future work.

As both  $\{\vec{c}_{obs}\}$  and  $\{\vec{c}_{true}\}$  are unordered sets, the method should be permutation equivariant. To achieve this, VIPR employs the transformer architecture [64, 65], using both the transformer encoders and decoders to extract information from the  $\{\vec{c}_{obs}\}$  and infer  $\{\vec{c}_{true}\}$ . For learning  $p(\{\vec{c}_{true}\}|N_{true}, S, \{\vec{c}_{obs}\}, \mu)$ , where  $N_{true}$  represents the number of ground-truth jet constituents, a conditional diffusion scheme [39–41, 45] is used. To obtain the full density  $p(\{\vec{c}_{true}\}|S, \{\vec{c}_{obs}\}, \mu)$ , a conditional normalizing flow is trained to approximate  $p(N_{true}|S, \{\vec{c}_{obs}\}, \mu)$ .

In diffusion, known gaussian noise is added to data with a some amount of strength defined by  $\sigma$ , and then the network  $F_\theta$  is trained to remove the added gaussian noise given the noisy data and the amount  $\sigma$ .

During training  $\sigma$  is sampled from a distribution described in Ref. [41], whereas during generation, pure gaussian noise is sampled and the network performs iterative denoising steps to generating  $\{\vec{c}_{true}\}$  of a true jet ( $j_{true}$ ). The number of iterative denoising steps are chosen beforehand and the number of steps defines the linearly spaced values of  $\sigma$ . Using the same observed properties, multiple samples can be generated from noise to obtain the posterior distribution.

In this study, during training each  $\{\vec{c}_{true}\}$  will be perturbed by a different amount gaussian distribution controlled by the strength  $\sigma$ .

During training, the maximum number of  $\{\vec{c}_{true}\}$  and  $\{\vec{c}_{obs}\}$  are set to 175 and 400 respectively. Summary variables for the entire observed jet ( $j_{obs}$ ) are used as conditions  $S$  to the network; these are the observed jet pseudorapidity  $\eta$ , azimuthal angle  $\phi$ , momentum transverse to the proton beams  $p_T$ , and the mass  $m$  of the observed jet.

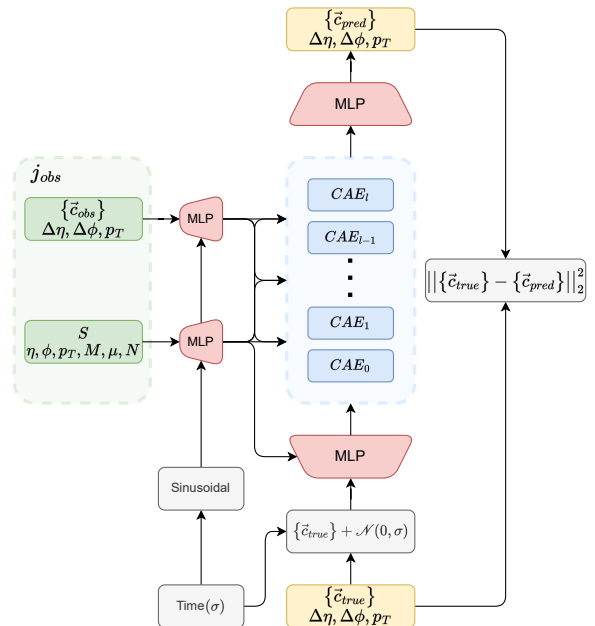


FIG. 1: The training scheme used in VIPR with  $\{\vec{c}_{obs}\}$  in the green box,  $\{\vec{c}_{true}\}$  and  $\{\vec{c}_{pred}\}$  in yellow boxes.

Cross attention encoders are shown in blue with standard MLPs in red. Both with trainable parameters.

The gray boxes indicate transformations that are non-trainable.

#### Architecture

The full diffusion architecture for VIPR is depicted in Fig. 1, where multiple cross attention encoder (CAE) blocks are stacked together to improve the fidelity of the transformation and to facilitate conditional message passing from  $\{\vec{c}_{obs}\}$  to  $\{\vec{c}_{true}\}$ . The Mean Squared Error (MSE) is used as the loss function, which minimises the difference between  $\{\vec{c}_{true}\}$  and  $\{\vec{c}_{pred}\}$ . All features are projected into a higher-dimensional space using multi-layer perceptrons (MLPs). The embedded features are afterwards passed into the CAE blocks.

A CAE block is shown in Fig. 2 and comprises two transformer encoders used to derive corrections within each point-cloud and a transformer decoder used for message passing between the two point-clouds. Both encoder

and decoders follow the architecture described in Ref [65]. Additional scalar information about the jet properties are concatenated internally in the MLP within the transformer layers.

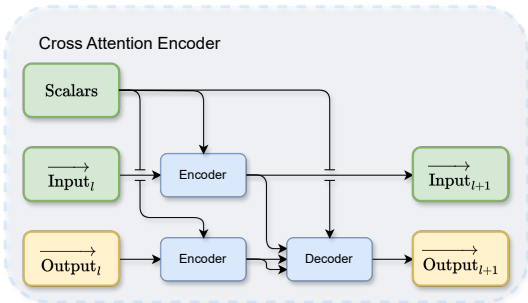


FIG. 2: The cross attention encoder (CAE) used iteratively within the VIPR (Fig. 1). It consists of two transformer encoders and a single transformer decoder following Ref [65]. Scalar variables are concatenated into the MLPs within each transformer layer. The color of the boxes indicates the type of information and follows the coloring from Fig. 1

#### IV. RESULTS

To assess the performance of VIPR, we look at its ability to obtain the correct jet  $p_T$ , invariant mass, and several jet substructure observables that are known to be useful for top-jet identification at a hadron collider: the ratio of the jet 2-subjettiness to the 1-subjettiness ( $\tau_{21}$ ) as well as the 3- to 2-subjettiness ratio ( $\tau_{32}$ ) [66]; the ratio of the three-point energy correlation function to the third power of the 2-point energy correlation function, as suggested in Ref. [67] ( $D_2$ ); and the square-root of the scale of the first and second  $k_t$  splittings ( $d_{12}$  and  $d_{23}$ ) [68]. The anti- $k_t$  jet clustering algorithm with radius parameter of  $R = 1.0$  is used to build jets of stable particles that fall within  $|\eta| < 2.5$ .

The SOFTDROP technique [18], which has become a standard at the LHC experiments, is used as the benchmark for comparison; we use the implementation from

Ref [69]. As VIPR is designed to remove pile-up from a single jet, we do not make comparisons to event level approaches, although it should be noted that these could be combined with VIPR by applying them before jet clustering.

The SOFTDROP algorithm has two hyperparameters,  $z_{\text{cut}}$  and  $\beta$ , controlling the sensitivity to soft and wide-angle radiation. Soft radiation is removed by increasing  $z_{\text{cut}}$  whereas decreasing  $\beta$  removes wide-angle radiation. We sweep  $z_{\text{cut}} = [0.05, 0.1, 0.15]$  and  $\beta = [0, 0.5, 1, 2]$ , motivated by choices in Ref [18, 70, 71] and find  $z_{\text{cut}} = 0.05$  and  $\beta = 2$  to give the minimize the bias and achieve the narrowest distribution across most quantities tested.

In Fig. 3, we show an example of an  $j_{\text{obs}}$  event with the ground truth in black circles and pile-up in red dots. Next to it is the same event but after applying SOFTDROP or VIPR for pile-up removal. For this event, we only sample a single sample from the posterior generated by VIPR, however, more samples of the posterior for that event can be seen in the appendix. From these figures, we see that the VIPR sample approximates the ground-truth much more accurately than the alternatives.

##### A. Performance of single jet reconstruction

For comparing the jet  $p_T$ , invariant mass, and substructure quantities, we use the relative error (RE) between the predicted and truth, defined as  $\text{RE} = \frac{\hat{x} - x}{x}$ , where  $\hat{x}$  is the predicted or generated value and  $x$  is the truth. The RE performance is assessed by drawing a single sample from the posterior of 100,000 individual  $j_{\text{obs}}$ , where the pile-up distribution follow a normal distribution of  $\mu$  with mean and standard deviation of 200 and 50, respectively:  $\mathcal{N}(\mu = 200, \sigma = 50)$ .

The RE of the jet  $p_T$ , invariant mass, and substructure observables can be seen in Fig. 4. Across all observables, VIPR has a substantially narrower RE distribution than SOFTDROP. The RE distribution of VIPR is also centered around zero, indicating that VIPR is unbiased, whereas

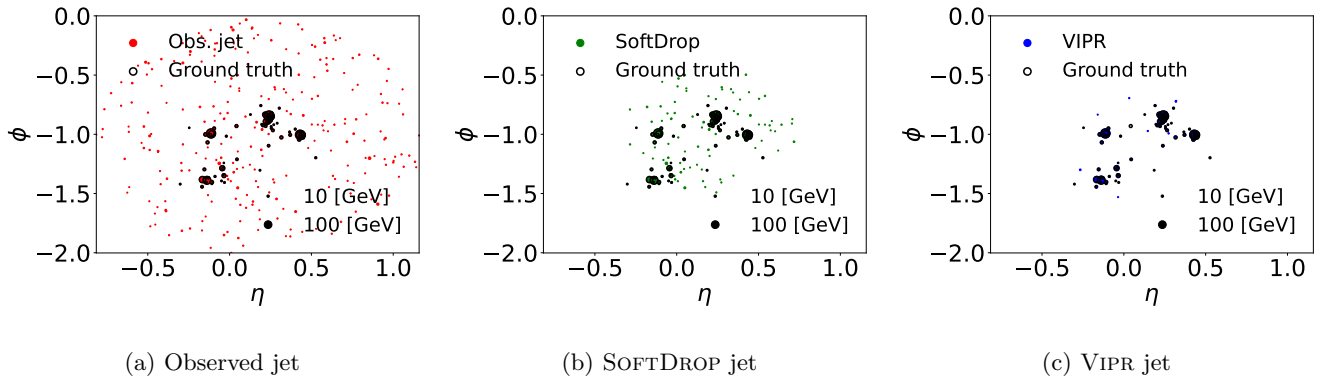


FIG. 3: Scatter plots showing the constituents of the observed  $\{\vec{c}_{obs}\}$ , SOFTDROP, and VIPR jets in the  $\eta$  and  $\phi$  plane, with constituent  $p_T$  indicated by the area of the solid circle. The black unfilled circles show the ground truth jet constituents  $\{\vec{c}_{true}\}$ . The VIPR jet is one sample taken from  $p(\{\vec{c}_{true}\}|S, \{\vec{c}_{obs}\}, \mu)$ . The observed jet is generated using a pile-up of  $\mu = 200$ .

SOFTDROP has a bias towards overprediction.

### B. Performance vs $\mu$

We evaluate the performance as a function of  $\mu \in [50, 60, 70, 80, 90, 100, 150, 200, 250, 300]$  by performing pile-up removal where a single prediction is generated from 10,000 different observed jets. We assess the bias (median) and interquartile range ( $IQR = \frac{Q_3 - Q_1}{1.349}$ ) of the RE distributions, where  $Q_1$  and  $Q_3$  are the 25% and 75% quantiles, respectively. Instead of visualising the 12 different SOFTDROP settings, we distill the information and visualise the envelope of the collection of SOFTDROP settings, rather than the 12 individual lines, with the best SOFTDROP setting in dashed green. The IQR of the RE as a function of  $\mu$  can be seen in Fig. 5. It is expected that with increasing  $\mu$ , the IQR increases as the jet becomes noisier from pile-up. Looking at Fig. 5, both  $j_{obs}$  and SOFTDROP are sensitive to this increase; however, VIPR is robust to increasing  $\mu$  as its IQR stays constant throughout the tested  $\mu$  range.

The bias as a function of  $\mu$  can be seen in Fig. 6. Across all observables, VIPR is centered at zero and remains consistent as a function of  $\mu$ , meaning there is no shift in the

RE as a function of  $\mu$ . On the other hand, SOFTDROP increases with increasing  $\mu$  and has larger biases than VIPR across various  $\mu$  values.

### C. Coverage

VIPR distinguishes itself from other pile-up removal methods due to its variational inference nature. Consequently, for each  $j_{obs}$ , VIPR can generate its posterior to establish the empirical coverage and verify whether VIPR is underconfident, overconfident, or correctly calibrated.

To obtain VIPR's posterior of a single  $j_{obs}$ , we sample from VIPR 512 times conditioned on the same  $j_{obs}$  to generate its posterior. We repeat this procedure for 2,000 different  $j_{obs}$  to generate a total of 2,000 posteriors. To assess the coverage, we calculate the quantile of the  $j_{true}$  observables for each of the generated posteriors.

The truth quantiles across the generated posteriors can be seen in Fig. 7, and they should be uniformly distributed to be correctly calibrated.

In Fig. 8, we show the integral of the posterior truth quantiles in Fig. 7. Across the observables, we see a slight underconfidence in VIPR, meaning the coverage properties will be slightly conservative; this is usually preferable

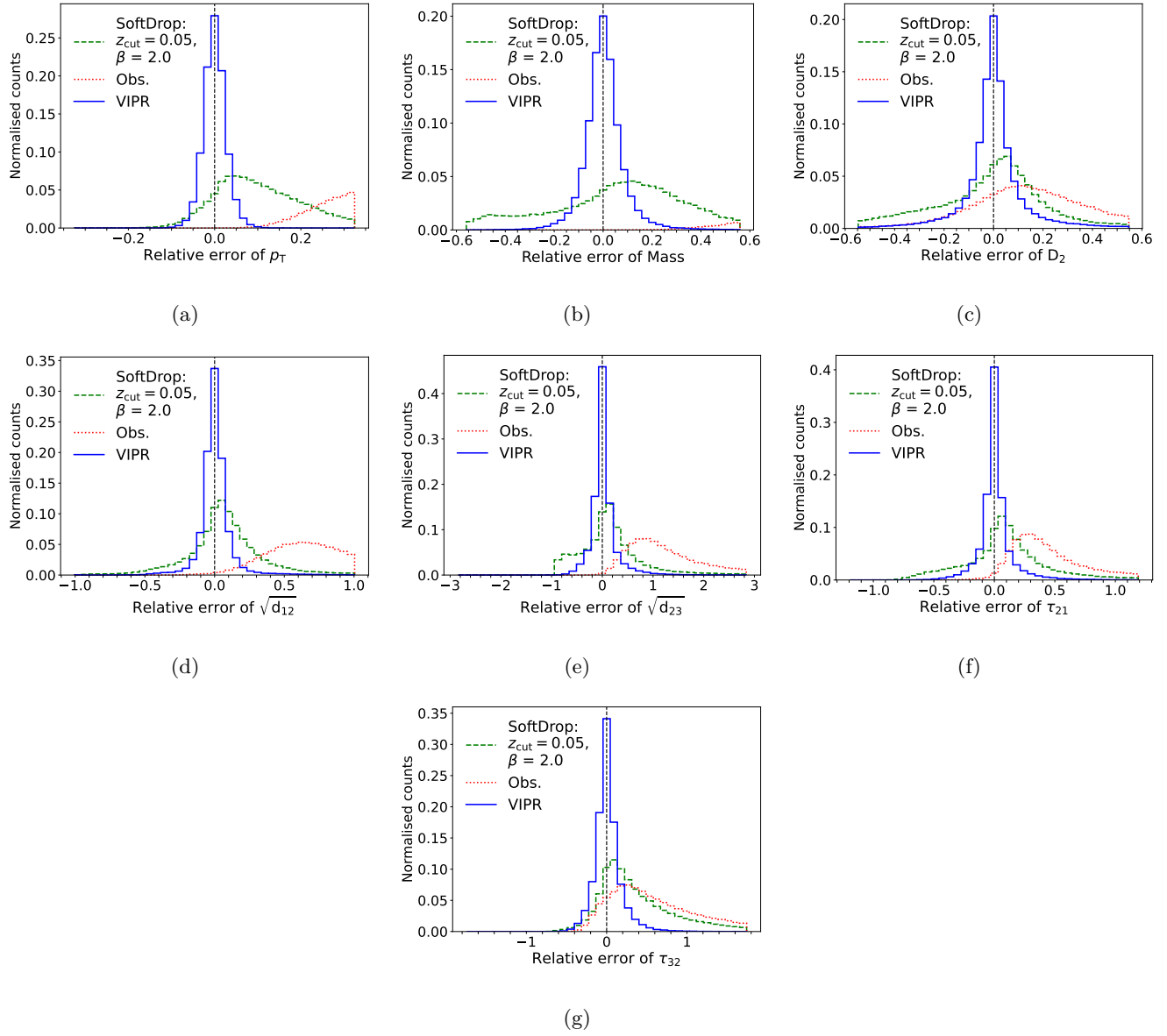


FIG. 4: Comparisons of the RE between observed (red), SOFTDROP (green) and VIPR (blue) in  $p_T$ , mass and substructure quantities. Ideally, the RE distribution should be symmetric and as close to a delta peak at zero as possible. The observed jet is generated using a pile-up distribution of  $\mathcal{N}(\mu = 200, \sigma = 50)$ .

to an overconfident procedure.

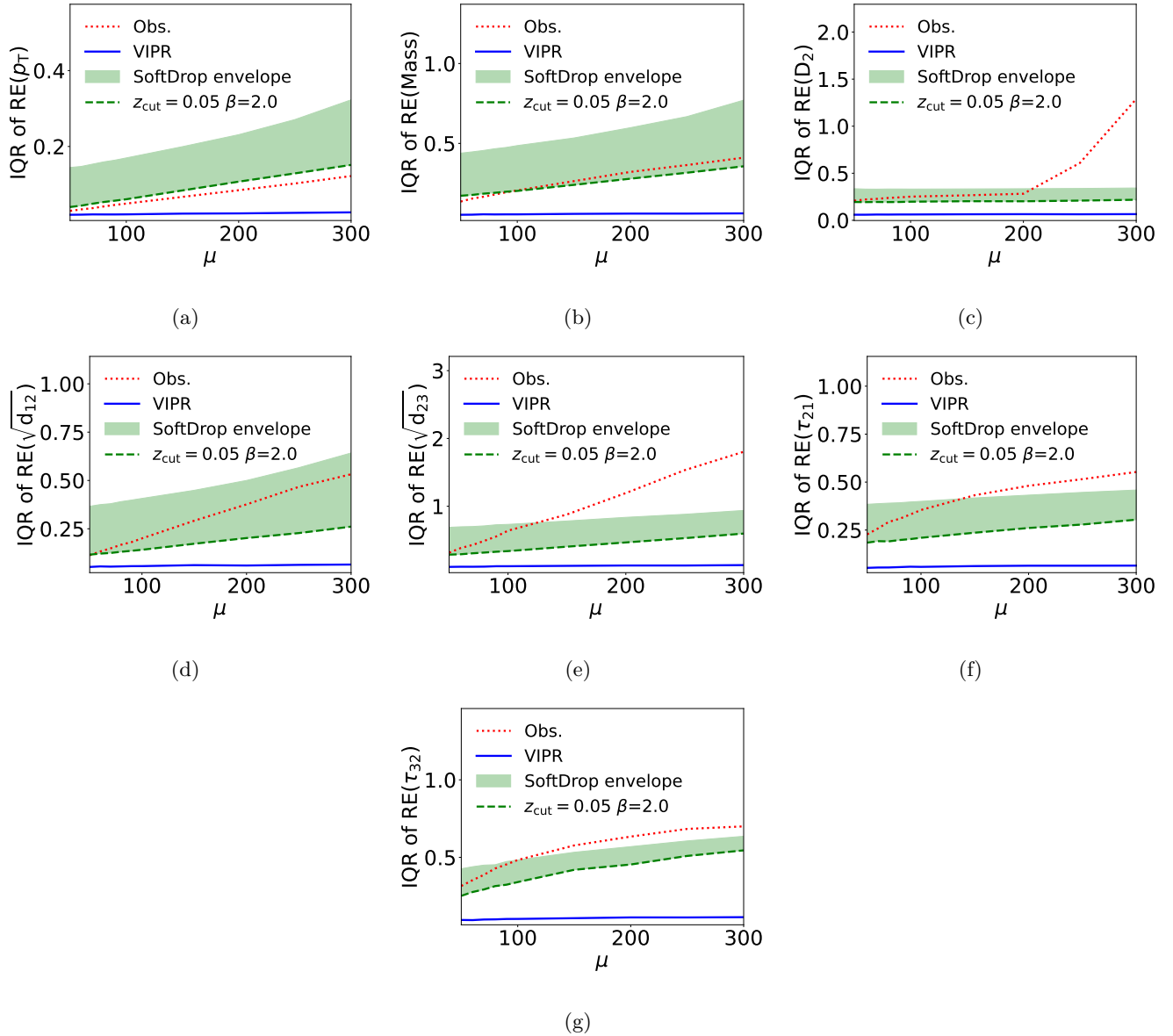


FIG. 5: Comparisons of the IQR of the RE as a function of  $\mu$  for various  $p_T$ , mass, and substructure variables. The IQR measures the width of the distribution. Ideally, the IQR should be as close to zero as possible and remain constant as a function of  $\mu$ . If the IQR remains constant as a function of  $\mu$ , it indicates that the pile-up removal method is robust towards increasing pile-up. The envelope of a scan of SOFTDROP settings is shown with the best resulting parameters in dashed green.

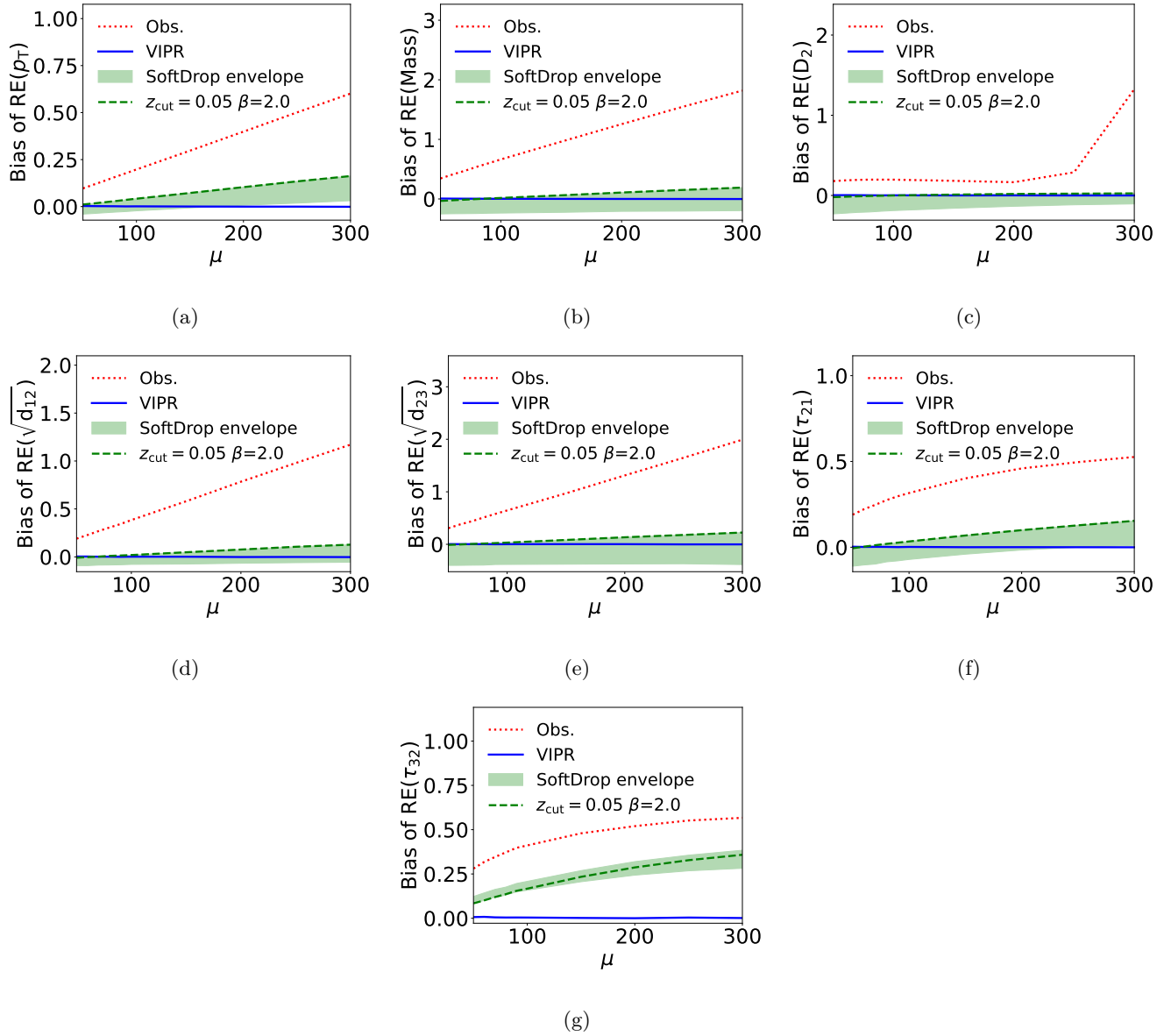


FIG. 6: Comparisons of the bias of the RE as a function of  $\mu$  for various  $p_T$ , mass, and substructure variables. The bias measures the median of the distribution. Ideally, the bias should be as close to zero as possible and remain constant as a function of  $\mu$ . If the bias remains constant as a function of  $\mu$ , it indicates that the pile-up removal method is robust towards increasing pile-up. The envelope of a scan of SOFTDROP settings with the best resulting parameters is shown with the dashed green.

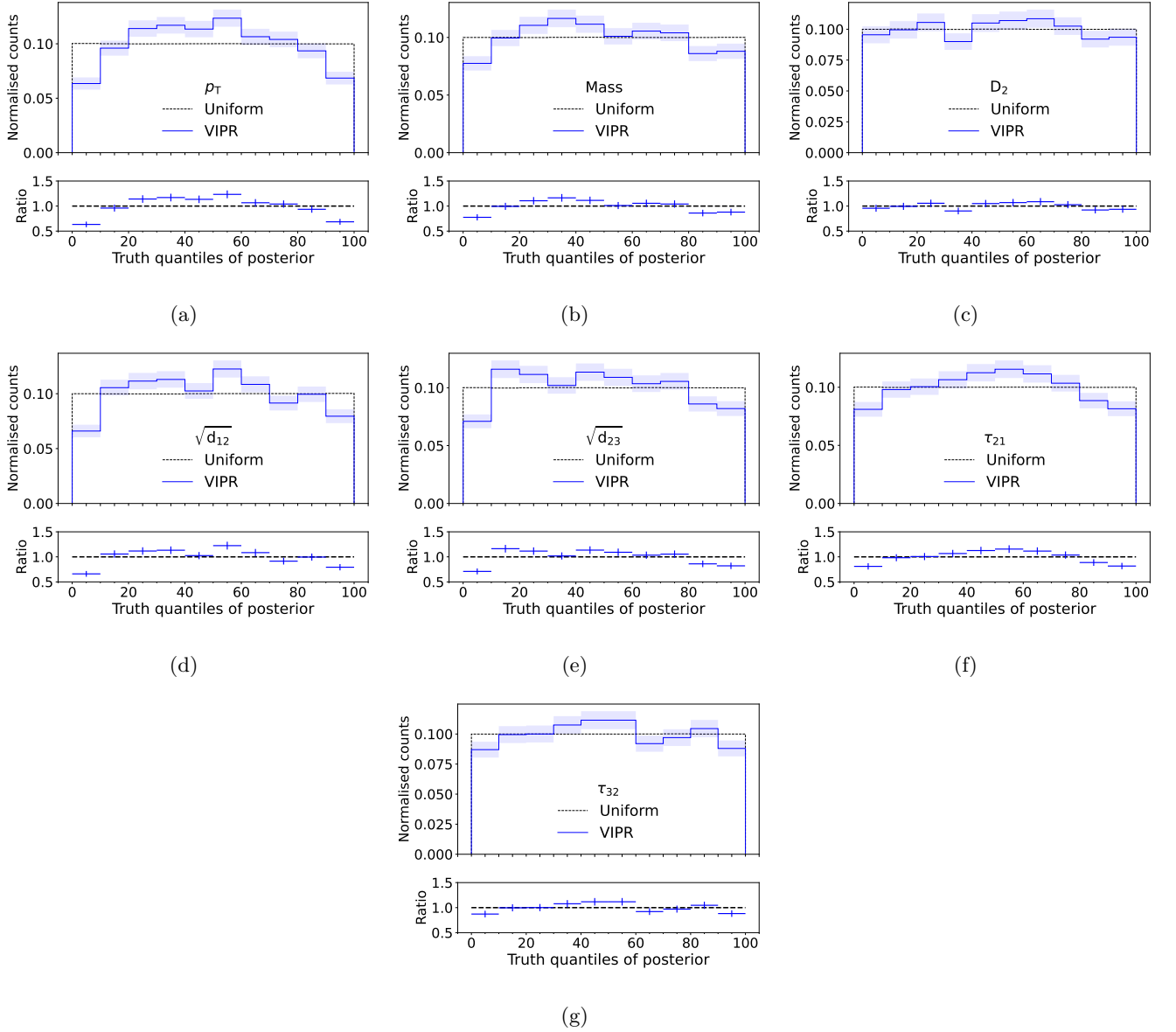


FIG. 7: Comparisons between the ideal uniform posterior truth quantile and the posterior truth quantile of VIPR in  $p_T$ , mass, and substructure variables. The posteriors have been generated by sampling a single  $j_{obs}$  512 times from the base distribution. This procedure has been repeated 2,000 times for different  $j_{obs}$  to generate the posterior truth quantiles. The single  $j_{obs}$  is generated using a pile-up distribution of  $\mathcal{N}(\mu = 200, \sigma = 0)$ . Ideally, the quantiles should be distributed uniformly on the generated posteriors to indicate that the model is correctly calibrated.

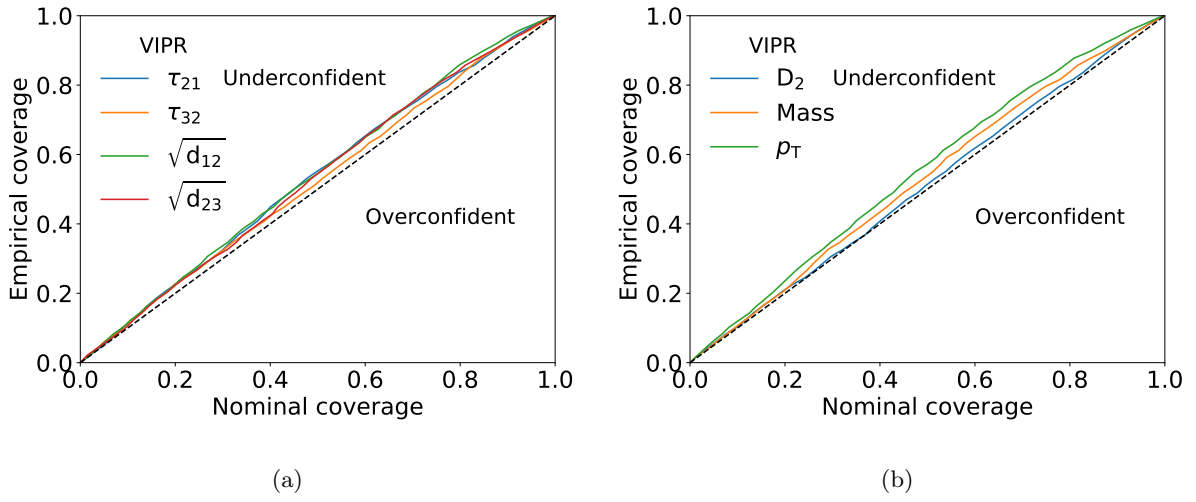


FIG. 8: Comparison between the ideal coverage and the VIPR coverage in  $p_T$ , mass and substructure variables. The coverage is calculated by integrating from the median and out over the posterior truth quantiles (Fig. 7). Ideally, the coverage should follow the black dashed line. Being above the black line indicates underconfidence, while being below it indicates overconfidence of the model.

## V. CONCLUSIONS

In this work we have introduced VIPR, a variational approach for pile-up removal by solving the inverse problem using diffusion models. VIPR is trained to generate a  $j_{true}$  from a noisy  $j_{obs}$  with pile-up attributes at the constituent level. The performance of VIPR has been evaluated on boosted top-quark jets under various pile-up levels. VIPR significantly outperforms the SOFTDROP technique in pile-up removal. In addition to state-of-the-art performance, VIPR can generate the posterior distribution of  $j_{true}$  given  $j_{obs}$ . Our results show that VIPR accurately reconstructs jet substructure, although with a slight under-confidence.

VIPR is designed for use during the high luminosity phase at the LHC, where it is anticipated to reach  $\langle\mu\rangle$  at

the level of 200 [12, 72]. It is trained with a pile-up distribution of  $\mathcal{N}(\mu = 200, \sigma = 50)$ , and we have evaluated its performance over a wide range of  $\langle\mu\rangle$  values. VIPR demonstrates robust performance across different pile-up levels.

## ACKNOWLEDGEMENTS

The MA, TG, and JAR would like to acknowledge funding through the SNSF Sinergia grant CR-SII5\_193716 “Robust Deep Density Models for High-Energy Particle Physics and Solar Flare Analysis (RODEM)” and the SNSF project grant 200020\_212127 “At the two upgrade frontiers: machine learning and the ITk Pixel detector”. CP acknowledges support through STFC consolidated grant ST/W000571/1.

- 
- [1] L. Evans and P. Bryant, LHC Machine, JINST **3**, S08001.
- [2] G. Aad *et al.* (ATLAS), Luminosity determination in  $pp$  collisions at  $\sqrt{s} = 13$  TeV using the ATLAS detector at the LHC, Eur. Phys. J. C **83**, 982 (2023), arXiv:2212.09379 [hep-ex].
- [3] A. Hayrapetyan *et al.* (CMS), Luminosity determination using Z boson production at the CMS experiment, Eur. Phys. J. C **84**, 26 (2024), arXiv:2309.01008 [hep-ex].
- [4] M. Aaboud *et al.* (ATLAS), Measurement of the Inelastic Proton-Proton Cross Section at  $\sqrt{s} = 13$  TeV with the ATLAS Detector at the LHC, Phys. Rev. Lett. **117**, 182002 (2016), arXiv:1606.02625 [hep-ex].
- [5] A. M. Sirunyan *et al.* (CMS), Measurement of the inelastic proton-proton cross section at  $\sqrt{s} = 13$  TeV, JHEP **07**, 161, arXiv:1802.02613 [hep-ex].
- [6] S. Navas *et al.* (Particle Data Group), Review of particle physics, Phys. Rev. D **110**, 030001 (2024).
- [7] G. Aad *et al.* (ATLAS), The ATLAS trigger system for LHC Run 3 and trigger performance in 2022, JINST **19** (06), P06029, arXiv:2401.06630 [hep-ex].
- [8] V. Khachatryan *et al.* (CMS), The CMS trigger system, JINST **12** (01), P01020, arXiv:1609.02366 [physics.ins-det].
- [9] T. A. Collaboration, The atlas experiment at the cern large hadron collider, Journal of Instrumentation **3** (08), S08003.
- [10] T. C. collaboration (CMS), The CMS experiment at the CERN LHC. The Compact Muon Solenoid experiment, JINST **3**, S08004, also published by CERN Geneva in 2010.
- [11] *Preliminary analysis of the luminosity calibration for the ATLAS 13.6 TeV data recorded in 2023*, Tech. Rep. (CERN, Geneva, 2024) all figures including auxiliary figures are available at <https://atlas.web.cern.ch/Atlas/GROUPS/PHYSICS/PUBNOTES/DAPR-PUB-2024-001>.
- [12] I. Zurbano Fernandez *et al.*, *High-Luminosity Large Hadron Collider (HL-LHC): Technical design report*, edited by I. Béjar Alonso, O. Brüning, P. Fessia, L. Rossi, L. Taviani, and M. Zerlauth, Vol. 10/2020 (2020).
- [13] M. Aaboud *et al.* (ATLAS), Reconstruction of primary vertices at the ATLAS experiment in Run 1 proton-proton collisions at the LHC, Eur. Phys. J. C **77**, 332 (2017), arXiv:1611.10235 [physics.ins-det].
- [14] *Performance of the ATLAS Inner Detector Track and Vertex Reconstruction in the High Pile-Up LHC*

- Environment*, Tech. Rep. (CERN, Geneva, 2012) all figures including auxiliary figures are available at <https://atlas.web.cern.ch/Atlas/GROUPS/PHYSICS/CONFNOTES/ATLAS-CONF-2012-042>.
- [15] G. P. Salam, Towards Jetography, *Eur. Phys. J. C* **67**, 637 (2010), arXiv:0906.1833 [hep-ph].
- [16] M. Cacciari, G. P. Salam, and G. Soyez, SoftKiller, a particle-level pileup removal method, *The European Physical Journal C* **75** (2015).
- [17] D. Bertolini, P. Harris, M. Low, and N. Tran, Pileup Per Particle Identification, *JHEP* **10**, 059, arXiv:1407.6013 [hep-ph].
- [18] A. J. Larkoski, S. Marzani, G. Soyez, and J. Thaler, Soft drop, *Journal of High Energy Physics* **2014** (2014).
- [19] G. Soyez, G. P. Salam, J. Kim, S. Dutta, and M. Cacciari, Pileup subtraction for jet shapes, *Phys. Rev. Lett.* **110**, 162001 (2013), arXiv:1211.2811 [hep-ph].
- [20] D. Krohn, M. D. Schwartz, M. Low, and L.-T. Wang, Jet Cleansing: Pileup Removal at High Luminosity, *Phys. Rev. D* **90**, 065020 (2014), arXiv:1309.4777 [hep-ph].
- [21] P. Berta, M. Spousta, D. W. Miller, and R. Leitner, Particle-level pileup subtraction for jets and jet shapes, *JHEP* **06**, 092, arXiv:1403.3108 [hep-ex].
- [22] ATLAS Collaboration, Constituent-level pile-up mitigation techniques in ATLAS (2017).
- [23] A. M. Sirunyan *et al.* (CMS), Pileup mitigation at CMS in 13 TeV data, *JINST* **15** (09), P09018, arXiv:2003.00503 [hep-ex].
- [24] ATLAS Collaboration, Performance of pile-up mitigation techniques for jets in  $pp$  collisions at  $\sqrt{s} = 8$  TeV using the ATLAS detector, *Eur. Phys. J. C* **76**, 581 (2016), arXiv:1510.03823 [hep-ex].
- [25] ATLAS Collaboration, Identification and rejection of pile-up jets at high pseudorapidity with the ATLAS detector, *Eur. Phys. J. C* **77**, 580 (2017), [Erratum: *Eur.Phys.J.C* **77**, 712 (2017)], arXiv:1705.02211 [hep-ex].
- [26] P. T. Komiske, E. M. Metodiev, B. Nachman, and M. D. Schwartz, Pileup Mitigation with Machine Learning (PUMML), *JHEP* **12**, 051, arXiv:1707.08600 [hep-ph].
- [27] J. Arjona Martínez, O. Cerri, M. Pierini, M. Spiropulu, and J.-R. Vlimant, Pileup mitigation at the Large Hadron Collider with graph neural networks, *Eur. Phys. J. Plus* **134**, 333 (2019), arXiv:1810.07988 [hep-ph].
- [28] S. Carrazza and F. A. Dreyer, Jet grooming through reinforcement learning, *Phys. Rev. D* **100**, 014014 (2019), arXiv:1903.09644 [hep-ph].
- [29] B. Maier, S. M. Narayanan, G. de Castro, M. Goncharov, C. Paus, and M. Schott, Pile-up mitigation using attention, *Mach. Learn. Sci. Tech.* **3**, 025012 (2022), arXiv:2107.02779 [physics.ins-det].
- [30] T. Li, S. Liu, Y. Feng, G. Paspalaki, N. V. Tran, M. Liu, and P. Li, Semi-supervised graph neural networks for pileup noise removal, *Eur. Phys. J. C* **83**, 99 (2023), arXiv:2203.15823 [hep-ex].
- [31] C. H. Kim, S. Ahn, K. Y. Chae, J. Hooker, and G. V. Rogachev, Restoring original signals from pile-up using deep learning, *Nucl. Instrum. Meth. A* **1055**, 168492 (2023), arXiv:2304.14496 [physics.ins-det].
- [32] M. H. Seymour, Searches for new particles using cone and cluster jet algorithms: A Comparative study, *Z. Phys. C* **62**, 127 (1994).
- [33] J. M. Butterworth, A. R. Davison, M. Rubin, and G. P. Salam, Jet substructure as a new Higgs search channel at the LHC, *Phys. Rev. Lett.* **100**, 242001 (2008), arXiv:0802.2470 [hep-ph].
- [34] D. E. Kaplan, K. Rehermann, M. D. Schwartz, and B. Tweedie, Top Tagging: A Method for Identifying Boosted Hadronically Decaying Top Quarks, *Phys. Rev. Lett.* **101**, 142001 (2008), arXiv:0806.0848 [hep-ph].
- [35] G. Aad *et al.* (ATLAS), A search for  $t\bar{t}$  resonances in lepton+jets events with highly boosted top quarks collected in  $pp$  collisions at  $\sqrt{s} = 7$  TeV with the ATLAS detector, *JHEP* **09**, 041, arXiv:1207.2409 [hep-ex].
- [36] C. Collaboration, Measurement of boosted higgs bosons produced via vector boson fusion or gluon fusion in the  $h \rightarrow b\bar{b}$  decay mode using lh proton-proton collision data at  $\sqrt{s} = 13$  tev (2024), arXiv:2407.08012 [hep-ex].
- [37] A. J. Larkoski, G. P. Salam, and J. Thaler, Energy Correlation Functions for Jet Substructure, *JHEP* **06**, 108, arXiv:1305.0007 [hep-ph].
- [38] G. Aad *et al.* (ATLAS), Optimisation of large-radius jet reconstruction for the ATLAS detector in 13 TeV proton-proton collisions, *Eur. Phys. J. C* **81**, 334 (2021), arXiv:2009.04986 [hep-ex].

- [39] Y. Song *et al.*, Score-based generative modeling through stochastic differential equations, in *Proceedings of the International Conference on Learning Representations* (2021) 2011.13456.
- [40] L. Yang, Z. Zhang, Y. Song, S. Hong, R. Xu, Y. Zhao, W. Zhang, B. Cui, and M.-H. Yang, Diffusion models: A comprehensive survey of methods and applications, arXiv:2209.00796 [cs.LG] (2023).
- [41] T. Karras *et al.*, Elucidating the design space of diffusion-based generative models, in *Proceedings of Advances in Neural Information Processing Systems* (2022) 2206.00364.
- [42] V. Mikuni and B. Nachman, Score-based generative models for calorimeter shower simulation, *Phys. Rev. D* **106**, 092009 (2022).
- [43] E. Buhmann, S. Diefenbacher, E. Eren, F. Gaede, G. Kasieczka, A. Korol, W. Korcari, K. Krüger, and P. McKeown, CaloClouds: Fast Geometry-Independent Highly-Granular Calorimeter Simulation, arXiv:2305.04847 [physics.ins-det] (2023).
- [44] F. T. Acosta, V. Mikuni, B. Nachman, M. Arratia, K. Barish, B. Karki, R. Milton, P. Karande, and A. Angerami, Comparison of Point Cloud and Image-based Models for Calorimeter Fast Simulation, arXiv:2307.04780 [cs.LG] (2023).
- [45] M. Leigh, D. Sengupta, G. Quétant, J. A. Raine, K. Zoch, and T. Golling, PC-JeDi: Diffusion for Particle Cloud Generation in High Energy Physics, *SciPost Phys.* **16**, 018 (2023), arXiv:2303.05376 [hep-ph].
- [46] V. Mikuni, B. Nachman, and M. Pettee, Fast Point Cloud Generation with Diffusion Models in High Energy Physics, arXiv:2304.01266 [hep-ph] (2023).
- [47] A. Butter, N. Huetsch, S. P. Schweitzer, T. Plehn, P. Sorrenson, and J. Spinner, Jet Diffusion versus JetGPT – Modern Networks for the LHC, arXiv:2305.10475 [hep-ph] (2023).
- [48] A. Shmakov, K. Greif, M. Fenton, A. Ghosh, P. Baldi, and D. Whiteson, End-To-End Latent Variational Diffusion Models for Inverse Problems in High Energy Physics, arXiv:2305.10399 [hep-ex] (2023).
- [49] V. Mikuni and B. Nachman, High-dimensional and Permutation Invariant Anomaly Detection, arXiv:2306.03933 [hep-ph] (2023).
- [50] M. Leigh, D. Sengupta, J. A. Raine, G. Quétant, and T. Golling, Faster diffusion model with improved quality for particle cloud generation, *Phys.Rev.D* **109**, 10.1103/PhysRevD.109.012010 (2023), arXiv:2307.06836 [hep-ex].
- [51] E. Buhmann, C. Ewen, D. A. Faroughy, T. Golling, G. Kasieczka, M. Leigh, G. Quétant, J. A. Raine, D. Sengupta, and D. Shih, EPIC-ly Fast Particle Cloud Generation with Flow-Matching and Diffusion, arXiv:2310.00049 [hep-ph] (2023).
- [52] T. Heimel, N. Huetsch, F. Maltoni, O. Mattelaer, T. Plehn, and R. Winterhalder, The MadNIS Reloaded, arXiv:2311.01548 [hep-ph] (2023).
- [53] E. Buhmann, C. Ewen, G. Kasieczka, V. Mikuni, B. Nachman, and D. Shih, Full Phase Space Resonant Anomaly Detection, arXiv:2310.06897 [hep-ph] (2023).
- [54] D. Sengupta, M. Leigh, J. A. Raine, S. Klein, and T. Golling, Improving new physics searches with diffusion models for event observables and jet constituents, arXiv:2312.10130 [physics.data-an] (2023).
- [55] M. Leigh, J. A. Raine, K. Zoch, and T. Golling,  $\nu$ -flows: Conditional neutrino regression, *SciPost Phys.* **14**, 159 (2023), arXiv:2207.00664 [hep-ph].
- [56] J. A. Raine, M. Leigh, K. Zoch, and T. Golling, Fast and improved neutrino reconstruction in multi-neutrino final states with conditional normalizing flows, *Phys.Rev.D* **109**, 10.1103/PhysRevD.109.012005 (2023), arXiv:2307.02405 [hep-ph].
- [57] J. Alwall, R. Frederix, S. Frixione, V. Hirschi, F. Maltoni, O. Mattelaer, H. S. Shao, T. Stelzer, P. Torrielli, and M. Zaro, The automated computation of tree-level and next-to-leading order differential cross sections, and their matching to parton shower simulations, *JHEP* **07**, 079, 1405.0301.
- [58] Artoisenet, Pierre and others, Automatic spin-entangled decays of heavy resonances in Monte Carlo simulations, *JHEP* **03**, 15 (2013).
- [59] T. Sjöstrand, S. Ask, J. R. Christiansen, R. Corke, N. Desai, P. Ilten, S. Mrenna, S. Prestel, C. O. Rasmussen, and P. Z. Skands, An introduction to PYTHIA 8.2, *Comput.Phys.Commun.* **191**, 159 (2015), 1410.3012.
- [60] R. D. Ball, V. Bertone, S. Carrazza, C. S. Deans, L. Del Debbio, S. Forte, A. Guffanti, N. P. Hartland,

- J. I. Latorre, J. Rojo, and M. Ubiali, Parton distributions with LHC data, *Nucl.Phys.B* **867**, 244 (2013), 1207.1303.
- [61] A. Buckley, J. Ferrando, S. Lloyd, K. Nordström, B. Page, M. Rüfenacht, M. Schönherr, and G. Watt, LHAPDF6: parton density access in the LHC precision era, *Eur.Phys.J.C* **75**, 132 (2015), 1412.7420.
- [62] M. Cacciari, G. P. Salam, and G. Soyez, The anti- $k_t$  jet clustering algorithm, *JHEP* **04**, 063, 0802.1189.
- [63] M. Cacciari, G. P. Salam, and G. Soyez, FastJet User Manual, *Eur.Phys.J.C* **72**, 1896 (2012), 1111.6097.
- [64] A. Vaswani, N. Shazeer, N. Parmar, J. Uszkoreit, L. Jones, A. N. Gomez, L. Kaiser, and I. Polosukhin, Attention Is All You Need (2023), arXiv:1706.03762 [cs.CL].
- [65] Ruibin Xiong and Yunchang Yang and Di He and Kai Zheng and Shuxin Zheng and Chen Xing and Huishuai Zhang and Yanyan Lan and Liwei Wang and Tie-Yan Liu, On Layer Normalization in the Transformer Architecture (2020), arXiv:2002.04745 [cs.LG].
- [66] Thaler, Jesse and Van Tilburg, Ken, Identifying boosted objects with N-subjettiness, *Journal of High Energy Physics* **2011** (2011).
- [67] A. J. Larkoski, G. P. Salam, and J. Thaler, Energy correlation functions for jet substructure, *Journal of High Energy Physics* **2013**, 10.1007/jhep06(2013)108 (2013).
- [68] A. J. Larkoski, I. Moulton, and D. Neill, Power counting to better jet observables, *Journal of High Energy Physics* **2014**, 10.1007/jhep12(2014)009 (2014).
- [69] E. M. Rikab Gambhir, Patrick Komiske and J. Thaler, **EnergyFlow** (2024).
- [70] M. Aaboud *et al.* (ATLAS), Measurement of the Soft-Drop Jet Mass in pp Collisions at  $\sqrt{s} = 13$  TeV with the ATLAS Detector, *Phys. Rev. Lett.* **121**, 092001 (2018), arXiv:1711.08341 [hep-ex].
- [71] ATLAS Collaboration (ATLAS), Measurement of soft-drop jet observables in  $pp$  collisions with the ATLAS detector at  $\sqrt{s} = 13$  TeV, *Phys. Rev. D* **101**, 052007 (2020), arXiv:1912.09837 [hep-ex].
- [72] ATLAS Collaboration, "Expected performance of the ATLAS detector under different High-Luminosity LHC conditions" (2021), <https://cds.cern.ch/record/2776650>.
- [73] C. Durkan, A. Bekasov, I. Murray, and G. Papamakarios, Neural spline flows (2019), arXiv:1906.04032 [stat.ML].

## VI. APPENDIX

### VII. DATA DISTRIBUTIONS

Fig. 9 shows the kinematic distributions of the constituents in the observed jets with pile-up distribution of  $\mathcal{N}(\mu = 200, \sigma = 50)$  and the top jets. The transverse momentum, pseudorapidity and invariant mass are shown in Fig. 10. The  $\eta$  and  $\phi$  distribution of the  $j_{true}$  and  $j_{obs}$  are shown in Fig. 10. Here it can be seen that the observed jets contain substantially more low momentum constituents falling in a wider distribution within the jet. The increased constituent multiplicity also leads to a substantial increase in the observed jet  $p_T$  and invariant mass.

#### A. Single event generation

Fig. 11 show the marginal distribution of the substructure,  $p_T$  and invariant mass of the observed, SOFTDROP, VIPR and  $j_{true}$ . It is these distributions that is used to calculate the RE distribution in Fig. 4.

### VIII. ESTIMATE OF $p(N; j)$

To estimate the number constituents of the Top jet, we train a normalising flow [73] to estimate  $p(N_{true}|S, \{\vec{c}_{obs}\}, \mu)$  from the observed jet. To learn the distribution of  $N$ , the normalising flow is conditioned on the observed jet, the number of pile-up interactions  $\mu$  and summary quantities  $S$ . To dequantize the distribution of  $N$ , we add  $\mathcal{N}(0, 0.5)$  to the discrete  $N$  and when sam-

pling we round to the nearest integer. The performance of the normalising flow can be seen in Fig. 12.

### IX. GENERATED POSTERIORES FROM VIPR

Fig. 13 shows multiple examples of possible generated VIPR jets. Each of these are used to construct the posterior distribution of the jet variables.

## X. HYPERPARAMETER

### A. Diffusion

	Time embedding	Sinusoidal
Diffusion	Dimension	64
	Frequency range	[0.001, 80]
Train	EMA	0.999
	LR	0.005
	LR scheduler	warmup(step=100000)
	Batch size	256
Model	Hidden dimension	256
	Attention heads	16
	Activation function	GELU
	MLP upscale	2
	Number of CAE	2

TABLE I: Table of hyperparameters used for VIPR. The MLP is the standard MLP from Ref [64, 65]

## XI. FLOW

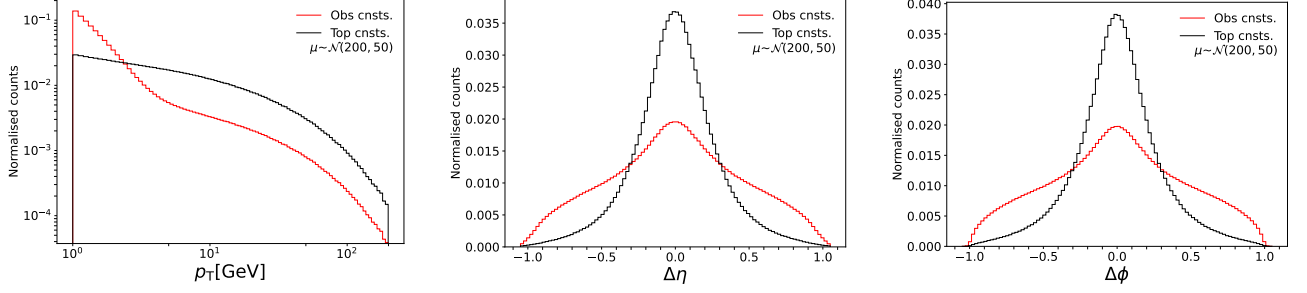


FIG. 9: Marginal distributions of  $p_T$ ,  $\Delta\eta$  and  $\Delta\phi$  on the constituent level across events for the observed jets with pile-up distribution of  $\mathcal{N}(\mu = 200, \sigma = 50)$  and the top jets.

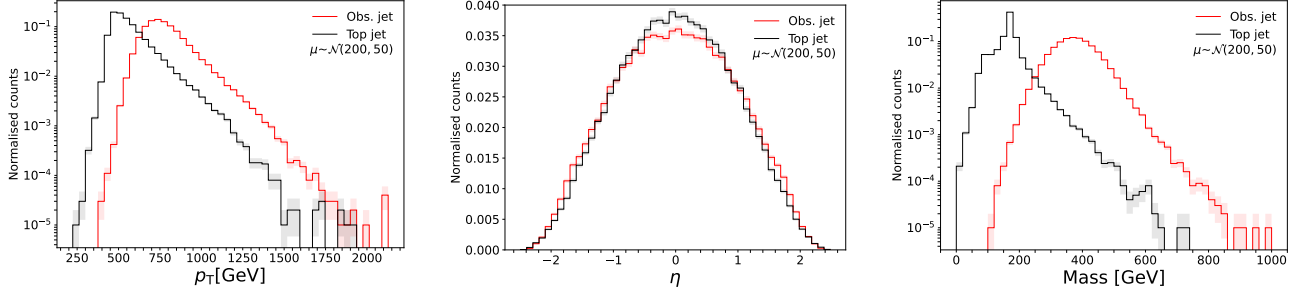


FIG. 10: Marginal distributions of  $p_T$ ,  $\eta$  and mass on the jet level across events for the observed jets with pile-up distribution of  $\mathcal{N}(\mu = 200, \sigma = 50)$  and the top jets.

CAE	Hidden dimension	256
	Number of encoders	2
	Number of decoders	2
	Attention heads	8
Train	Gradient clip	10
	LR	[0.0001, 1e-7]
	LR scheduler	CosineAnnealingLR
	Batch size	256
Flow	Context dimension	512
	Number of stacks	4
	Activation function	GELU
	Base distribution	Normal distribution
Flow	Transformation	RQS
	Number of bins	12
	Tail	Linear[-4,4]

TABLE II: Table of hyperparameters used for the flow used to estimate  $p(N; j)$ . The MLP hyperparameters are the same as in Table I.

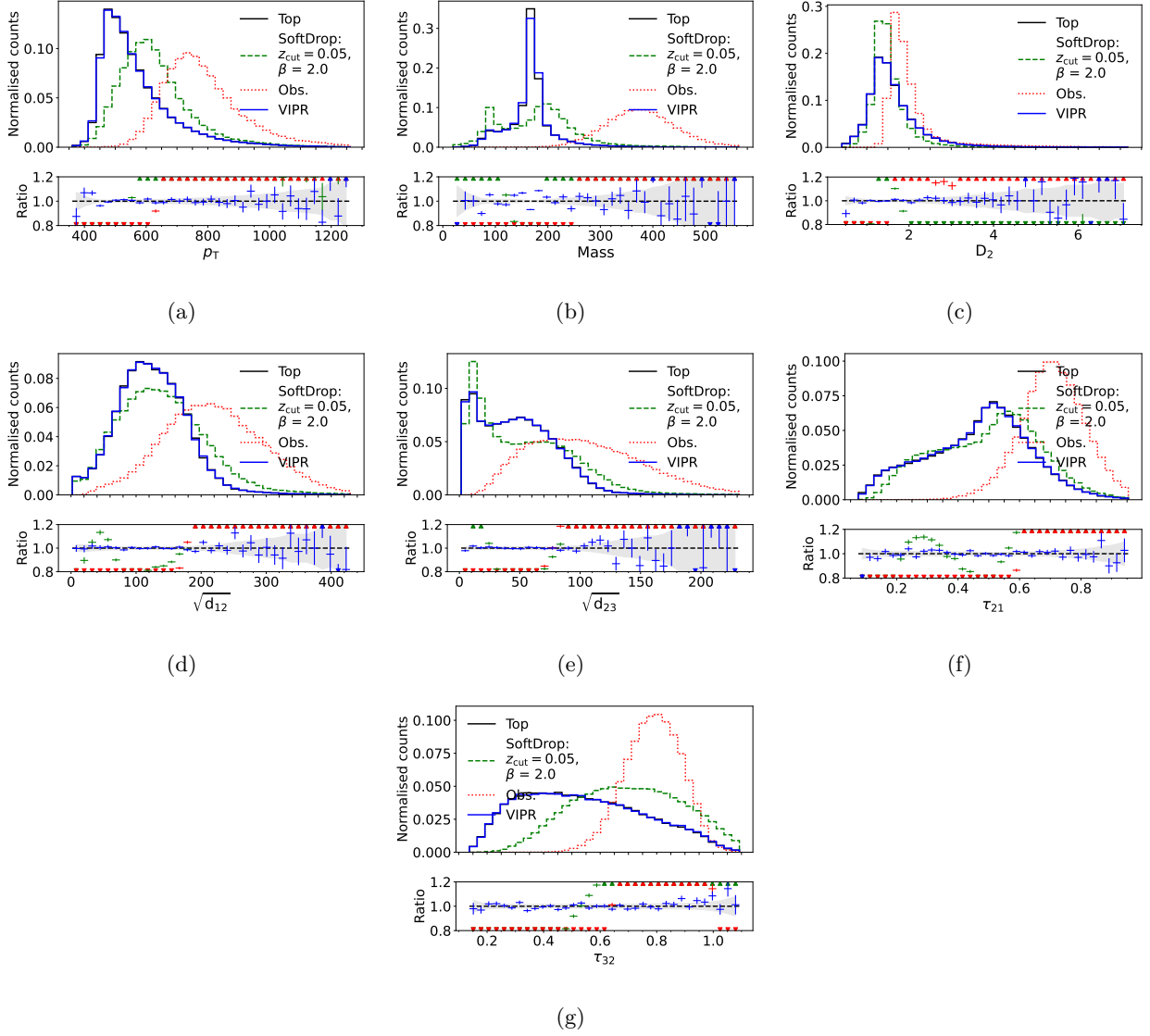


FIG. 11: Marginal distributions of the jet'  $p_T$ , mass and substructures observables of the ground truth, SOFTDROP, observed, and VIPR jets. The  $j_{obs}$  have been generated using pile-up distribution at  $\mathcal{N}(\mu = 200, \sigma = 50)$ .

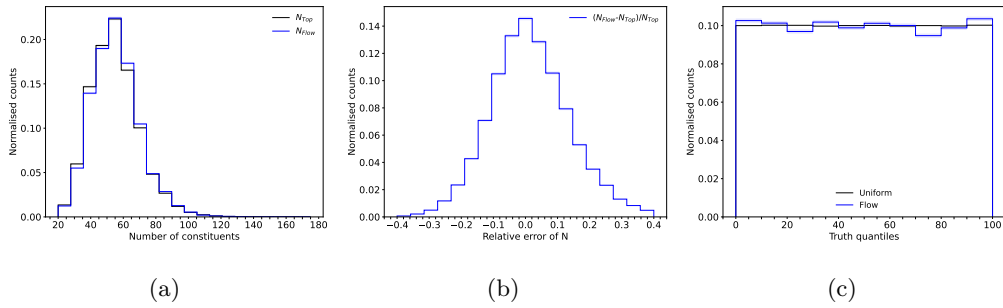


FIG. 12: (a) Comparisons between the flow generated  $N$  and the truth  $N$ . (b) RE of the flow generated  $N$ . (c) Posterior truth quantiles of the flow. In all three cases,  $\mathcal{N}(\mu = 200, \sigma = 50)$  is used as pile-up distribution.

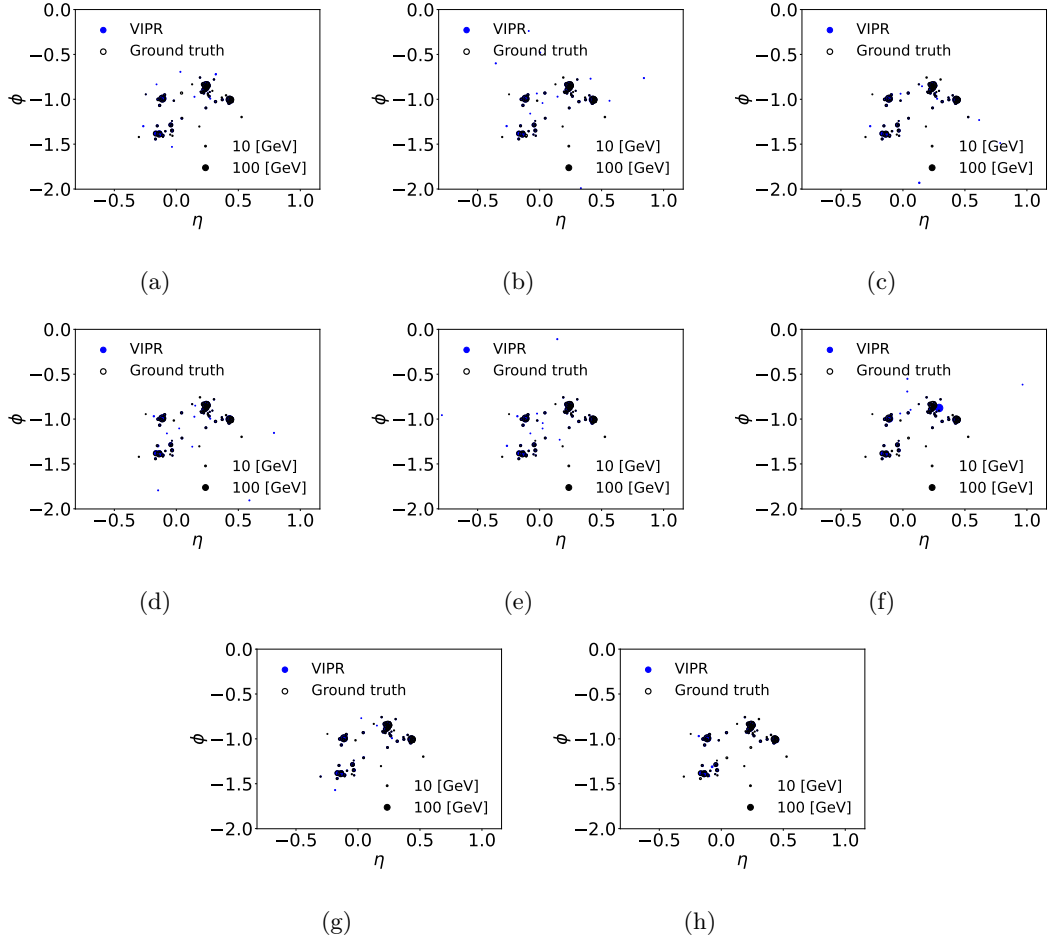


FIG. 13: Scatter plots shows multiple examples of generated VIPR jets on the constituent level in  $\eta$  and  $\phi$  plane, with  $p_T$  indicated by the area of the circle. All the generated jets are using the same observed jet. The black circle represents the ground truth constituents.